On the influence of initial geometry on the evolution of fluid filaments

K. Mahady, S. Afkhami, and L. Kondic

Citation: Physics of Fluids **27**, 092104 (2015); doi: 10.1063/1.4931086
View online: http://dx.doi.org/10.1063/1.4931086
View Table of Contents: http://scitation.aip.org/content/aip/journal/pof2/27/9?ver=pdfcov
Published by the AIP Publishing

Articles you may be interested in

Hydrodynamic cavitation in microsystems. II. Simulations and optical observations
Phys. Fluids **24**, 047101 (2012); 10.1063/1.3699067

Direct numerical simulation of the near-field dynamics of annular gas-liquid two-phase jets
Phys. Fluids **21**, 042103 (2009); 10.1063/1.3112740

Oscillatory convective structures and solutal jets originated from discrete distributions of droplets in organic alloys with a miscibility gap
Phys. Fluids **18**, 042105 (2006); 10.1063/1.2192531

Erratum: “The motion of a falling liquid filament” [Phys. Fluids 12, 550 (2000)]
Phys. Fluids **12**, 1881 (2000); 10.1063/1.870435

The motion of a falling liquid filament
Phys. Fluids **12**, 550 (2000); 10.1063/1.870261

Did your publisher get
18 MILLION DOWNLOADS in 2014?
AIP Publishing did.

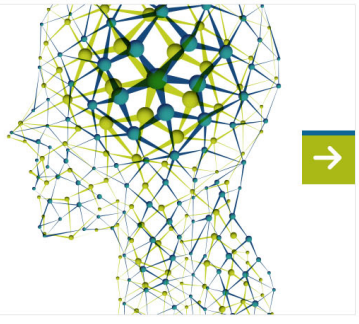

THERE'S POWER IN NUMBERS. Reach the world with AIP Publishing.

This article is copyrighted as indicated in the article. Reuse of AIP content is subject to the terms at: http://scitation.aip.org/termsconditions. Downloaded to IP: 128.235.83.176 On: Mon, 21 Sep 2015 16:48:41

CrossMark click for updates

PHYSICS OF FLUIDS **27**, 092104 (2015)

On the influence of initial geometry on the evolution of fluid filaments

K. Mahady, S. Afkhami, and L. Kondic
Department of Mathematical Sciences, New Jersey Institute of Technology, Newark, New Jersey 07102, USA

(Received 24 April 2015; accepted 6 August 2015; published online 21 September 2015)

In this work, the influence of the initial geometry on the evolution of a fluid filament deposited on a substrate is studied, with a particular focus on the thin fluid strips of nano-scale thickness. Based on the analogy to the classical Rayleigh–Plateau (R–P) instability of a free-standing fluid jet, an estimate of the minimal distance between the final states (sessile droplets) can be obtained. However, this numerical study shows that while the prediction based on the R–P instability mechanism is highly accurate for an initial perturbation of a sinusoidal shape, it does not hold for a rectangular waveform perturbation. The numerical results are obtained by directly solving fully three-dimensional Navier–Stokes equations, based on a Volume of Fluid interface tracking method. The results show that (i) rectangular-wave perturbations can lead to the formation of patterns characterized by spatial scales that are much smaller than what is expected based on the R–P instability mechanism; (ii) the nonlinear stages of the evolution and end states are not simply related, with a given end state resulting from possibly very different types of evolution; and (iii) a variety of end state shapes may result from a simple initial geometry, including one- and two-dimensional arrays of droplets, a filament with side droplets, and a one-dimensional array of droplets with side filaments. Some features of the numerical results are related to the recent experimental study by Roberts *et al.* ["Directed assembly of one- and two-dimensional nanoparticle arrays from pulsed laser induced dewetting of square waveforms," ACS Appl. Mater. Interfaces **5**, 4450 (2013)]. © *2015 AIP Publishing LLC.* [http://dx.doi.org/10.1063/1.4931086]

I. INTRODUCTION

Synthesis and assembly on the nano-scale is one of the most important goals of contemporary science and technology, see, e.g., Ref. 1. While there are a large number of examples involving a variety of different fluids where self and directed assemblies are relevant, we focus here on one particular example which is finding important applications: nano-scale metallic particles. These particles have been used as a basis for controlled growth of carbon nano-fibers,[2] with applications in numerous settings.[3] More generally, formation of nano-structures of metallic materials finds its role in applications which range from plasmonics to liquid crystal displays and solar cells.[4,5] For example, the size and distribution of metallic particles are known to be related to the coupling of surface plasmons to incident energy. Controlling this coupling has the potential for large increases in the yield of solar cell devices, see, e.g., Ref. 6; for this application, it is particularly important to be able to produce uniformly distributed and closely spaced metallic nano-particles.[7,8] One approach to produce nano-scale structures (metallic or not) with a desired size and distribution is to use naturally occurring forces that drive the evolution of the nano-structures in the liquid phase;[9] such an approach, if controlled, is significantly more efficient than to lithographically depositing individual particles. With metal films, a recently developed technique is the irradiation with laser pulses or electron-beams, leading to fast liquefaction. While in the liquid phase, the metal film becomes unstable and breaks up into droplets which solidify and remain on the substrate as solid particles. The understanding of this instability development is the focus of this paper. We note that while the particular problem involving liquid metals on nanoscale motivated this work, the

 ©2015 AIP Publishing LLC

This article is copyrighted as indicated in the article. Reuse of AIP content is subject to the terms at: http://scitation.aip.org/termsconditions. Downloaded to IP: 128.235.83.176 On: Mon, 21 Sep 2015 16:48:41

approach that we implement is general and it applies to any setup that allows for control of the initial geometry.

One commonly considered geometry in the experiments is the one of a filament deposited on a solid substrate. In the context of metal films, a liquid filament itself does not even have to be deposited: it is sufficient to deposit a metal strip of a rectangular cross section, liquefy it, and let the capillary forces drive the evolution. Such a setup has been recently demonstrated experimentally in Ref. 10, which considers a geometry consisting of long, thin, strips with thicknesses of tens of nanometers, widths of hundreds of nanometers, and lengths of tens of microns. When liquefied by laser pulses of typical duration of tens of nanoseconds, these strips quickly retract into filaments that then break up into droplets, where the spacing of the droplets is not uniform, but instead obeys a distribution consistent with the prediction of the classical Rayleigh–Plateau (R–P) analysis. This mechanism of breakup can be explained surprisingly well by an analogy with the R–P analysis of the breakup of a free standing fluid jet, modified by the presence of substrate, as discussed in Ref. 11. Following the analysis in Ref. 11, Ref. 10 shows that varying the width of the deposited metal strip by a sinusoidal perturbation of a well defined wavelength can be used to produce an array of uniformly spaced particles, as long as this imposed wavelength is unstable, based on the R–P instability analysis. They show that perturbing by stable (short) wavelengths leads to distances between the particles that are nonuniform and not related to the imposed perturbation. In this paper, we explore whether one could overcome this limitation by appropriately choosing the initial fluid geometry.

Before discussing this question further, we outline briefly the basic framework determining the stability of fluid jets. The classical R–P linear stability analysis (LSA) predicts that radial sinusoidal perturbations of a standing jet of radius R, with wavenumber $k = 2\pi/\lambda$, and small amplitude, grow or decay with the growth rate, ω, specified by

$$\omega^2 = \frac{\sigma}{\rho R^3}\left(kR(1-k^2R^2)\frac{I_1(kR)}{I_0(kR)}\right), \tag{1}$$

where σ is the surface tension, ρ the density, and I_0 and I_1 the modified Bessel functions.[12,13] This result predicts a critical wavelength, λ_c, below which modes are stable, as $2\pi R$[12] derives the growth rate when the effects of viscosity are ignored; we should note, however, that the critical wavenumber predicted based on the R–P analysis remains unchanged when considering viscous effects.[14] We also note that Eq. (1) applies to small amplitude varicose modes of any waveform, as these can be decomposed into sinusoidal component modes via a Fourier transform.

The presence of a substrate naturally modifies Eq. (1). Viscous and viscointertial limits of the dispersion relation for a filament on a substrate are derived by Ref. 15. The LSA based on long–wave (L–W) theory demonstrates that λ_c is modified only slightly by the presence of the substrate, showing a weak dependence on the contact angle (the angle at which the interface between the liquid and an ambient phase, such as a surrounding gas, meets a solid surface).[10,11,16,17] Several methods for calculating λ_c for a filament on a substrate are compared in Ref. 17; importantly, for a contact angle of $\pi/2$, the critical wavelength remains exactly the same as that predicted by the R–P analysis.

As mentioned above, the R–P driven breakup limits how closely spaced particles can be based on the critical wavelength. To overcome this limitation, in an experimentally focused study,[18] introduce a rectangular-wave type perturbation form. The initial geometry consists of a central strip of width w and height h, to which perpendicular protrusions are attached, with amplitude A_p, width w_p, and period λ_p, as illustrated in Fig. 1(b). Such a structure can be compared with a strip whose cross-sectional area is given by

$$\Omega_{\text{eff}} = h(w + 2A_p w_p/\lambda_p) = \Omega_0 + 2A_p h w_p/\lambda_p,$$

where Ω_0 is the cross-sectional area of the main strip (without protrusions), and Ω_{eff} is the average cross-sectional area obtained when the total amount of liquid (including protrusions) is distributed evenly over a wavelength λ_p. We call Ω_{eff} an effective cross-sectional area.

In Ref. 18, the initial condition shown in Fig. 1(b) was found to lead to two distinct end states, consisting of either one- or two-dimensional array of particles. Fig. 2 illustrates these end states. For smaller A_p, the end state is a one-dimensional array of particles whose centers are exactly at the location of the original rectangular-wave perturbations (Figs. 2(b), 2(d), and 2(f)). As A_p is

This article is copyrighted as indicated in the article. Reuse of AIP content is subject to the terms at: http://scitation.aip.org/termsconditions. Downloaded to IP: 128.235.83.176 On: Mon, 21 Sep 2015 16:48:41

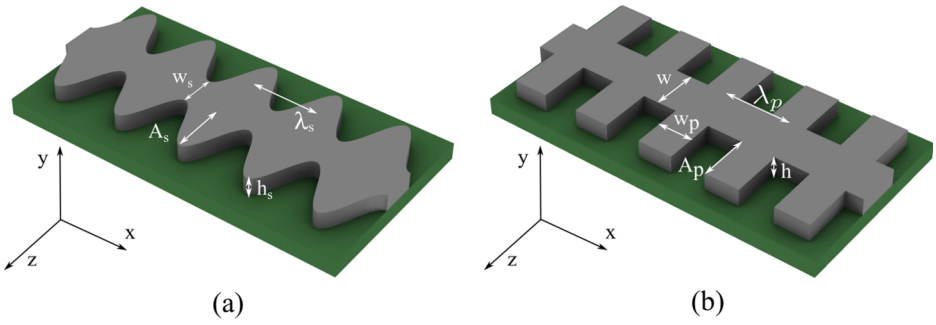

FIG. 1. Two perturbation geometries for assembling arrays of nano-particles: (a) sinusoidal initial geometry and (b) rectangular-wave initial geometry. The rectangular-wave geometry consists of a central strip of width w and height h; the perpendicular protrusions have an amplitude A_p, width w_p, and period λ_p.

increased, the end state transitions to a two-dimensional array of particles (Figs. 2(h) and 2(j)): one set of particles is located at the same locations as the one dimensional arrays of Figs. 2(b), 2(d), and 2(f), while two more sets of particles are located on either side. In the present paper, we focus on understanding the physical mechanisms that lead to the end states illustrated by Fig. 2, as well as to a variety of other possible end states that have not been observed in experiments yet. While the approach that we use is general and applies to any setup such that the initial geometry can be controlled, for definitiveness we choose the relevant length and time scales as well as material parameters corresponding to metal filaments of nano-scale thickness, as in Ref. 18. We computationally investigate the effects of varying parameters on conditions for which the breakup occurs and demonstrate that not only is it possible to destabilize the structure when $\lambda_p < \lambda_c(\Omega_{\text{eff}})$ but also even when $\lambda_p < \lambda_c(\Omega_0)$. That is, despite the additional liquid added into the system by the protrusions, we can actually induce the strip to break up with a period less than its own critical wavelength, leading, as a final outcome, to droplets spaced much closer than that would appear possible by considering the R–P predictions. This finding is surprising and also potentially very useful, since in many applications, it is desirable to have closely spaced particles.[19]

The rest of this paper is organized as follows. In Sec. II, we outline the simulation setup. The results are given in Sec. III, including description of the basic instability mechanism, classification

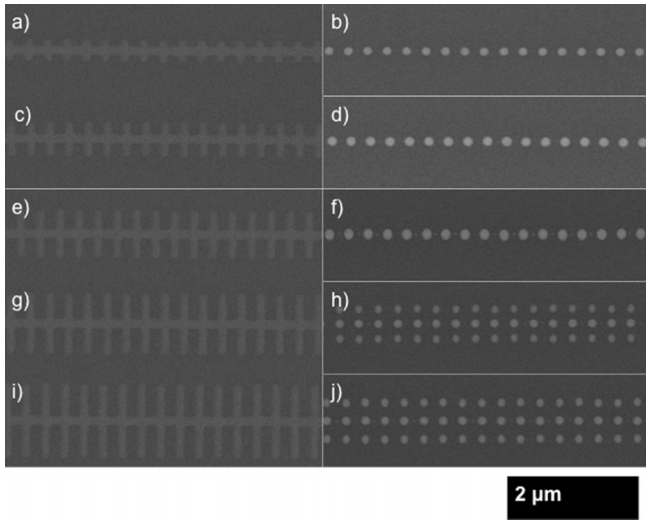

FIG. 2. Experimental images of the initial conditions (left column) and end states (right column) for the rectangular-wave geometry such as shown in Fig. 1. The film thickness is $h \approx 7$ nm. Here, the amplitude of perturbation, A_p, is increased, while all other parameters are kept the same. Reprinted with permission from Roberts *et al.*, ACS Appl. Mater. Interfaces **5**, 4450 (2013). Copyright 2013 American Chemical Society.

This article is copyrighted as indicated in the article. Reuse of AIP content is subject to the terms at: http://scitation.aip.org/termsconditions. Downloaded to IP: 128.235.83.176 On: Mon, 21 Sep 2015 16:48:41

of various end states uncovered by the simulations, and dependence of the results on the parameters defining the perturbations. In Sec. IV, we discuss in more details some crucial aspects of the instability mechanism. The conclusions and the outline of future work are presented in Sec. V.

II. SETUP

Figure 1(b) shows our initial geometry, which is a flat strip with a rectangular-wave edge perturbation similar to the one considered by Ref. 18. The geometry consists of what we refer to as a "central strip" defined by

$$\{(x,y,z)|\ -\infty < x < \infty,\ y < h,\ |z| < w/2\}$$

and "protrusions" defined by

$$\left\{(x,y,z)|\ |x - n\lambda_p| < w_p/2,\ y < h,\ |z| < (w/2 + A_p),\ \text{for}\ n \in \mathbb{Z}\right\}.$$

Throughout this paper, we take the central strip to be specified by $h = 10$ nm and $w = 100$ nm. As described above, experimental studies begin by depositing metal in prescribed geometries such as a strip with an edge perturbation and then liquefying these structures with laser pulses. While in the experiments, the metal geometries may be going through repeated melting and solidification, in the present work, we neglect the effects of phase change and furthermore assume that temperature variation of material parameters (viscosity, density, surface tension) is not crucial for the purpose of understanding the main mechanisms leading to instability. This approach is supported further by the fact that the constant temperature model has generally been very successful in modeling the breakup of nanometallic films.[10,11,18] These approximations are also motivated by our desire to focus on the influence of the initial geometry on instability development in a general setting. In the particular case of laser-irradiated metals, thermal simulations[10] suggest that the phase change itself happens on a very fast time scale. A simplified model addressed by Ref. 20 also indicates that the heating of nanometallic films takes place rapidly, leading to a sharp, short-lived peak in the temperature. In the present work, we are essentially assuming that during the time that the metal is in the liquid phase, we can ignore temperature variations. Of course, if the temperature of the metal is significantly higher than the melting temperature, one may expect a decrease of the viscosity and surface tension that may modify the results. We leave such considerations for future work and focus here on the influence of geometry on the development of the instability. Within present isothermal model, the evolution of the initial structure is thus governed by the Navier–Stokes (N–S) equations for an isothermal fluid. We consider an initial geometry that is far from equilibrium and rapidly evolves to what we refer to as its "end state."

As discussed in more detail below, the computational solver that we use requires the presence of two fluids, and therefore we consider two phases that are immiscible and incompressible, separated by an interface: metal in its liquid phase (referred to as "liquid") and the ambient phase. The governing equations under these assumptions become the two-phase N–S equations

$$\rho\left(\partial_t \mathbf{u} + \mathbf{u}\cdot\nabla\mathbf{u}\right) = -\nabla p + \nabla\cdot\left(\mu\left(\nabla\mathbf{u} + \nabla\mathbf{u}^T\right)\right) + \sigma\kappa\delta_s\mathbf{n}, \tag{2}$$

$$\nabla\cdot\mathbf{u} = 0, \tag{3}$$

where $\mathbf{u} = (u,v,w)$ is the velocity field, p the pressure, σ the surface tension, κ the interfacial curvature, δ_s a delta function centered on the interface, and $\mathbf{n}$ the unit normal to the interface. The viscosity, μ, and density, ρ, depend on the phase of the fluid, taking values of μ_l, ρ_l in the liquid phase and μ_a, ρ_a in the ambient phase. For our simulations, we use the physical values of liquid nickel (Ni) used in Ref. 18, so that $\rho_l = 7905$ kg/m^3, $\mu_l = 0.0047$ Pa s, and $\sigma = 1.781$ N/m. The values of μ_a and ρ_a are chosen to minimize the effects of the ambient phase; we discuss these values further when the numerical methods are described. We note that Eq. (2) does not include the effects of the disjoining pressure. Previous models of similar problems, based on long–wave theory, included the disjoining pressure to model partial wetting and the linear stability of the interface, as discussed by Ref. 11. In the present work, partial wetting is introduced differently (described below). Furthermore, we expect that the interfacial instability due to the disjoining pressure effects

This article is copyrighted as indicated in the article. Reuse of AIP content is subject to the terms at: http://scitation.aip.org/termsconditions. Downloaded to IP: 128.235.83.176 On: Mon, 21 Sep 2015 16:48:41

is weak compared to other effects; a rough estimate shows that the breakup time of a uniform 10 nm film by the disjoining pressure is considerably longer than the evolution time of the structures considered in the present work (see the linear stability analysis in Ref. 21). Our current model and computational methods were previously shown to result in good qualitative agreement when compared to the experimental results in Ref. 18.

On the solid substrate, we impose the Navier slip boundary condition

$$(u, w) = \Lambda \frac{\partial}{\partial y}(u, w), \tag{4}$$

where Λ is the slip length. Experimental results for various liquids and substrates have generally reported significant slip on surfaces with large contact angles,[22] with a range of possible slip lengths depending on the surface topography and chemistry.[23] Often, a slip length on the order of 100 nm is reported for systems with contact angles ranging from 95° to 105°.[22–24] Reference 25 also show that the slip is large in the present system by comparing the N–S solutions with molecular dynamics simulations of nano-scale metal films by Ref. 26. In this work, we briefly survey the effects of varying slip, but unless noted otherwise, we take $\Lambda = 60$ nm. This particular value of slip length is motivated by Ref. 18, where good agreement between the simulation results and the experimental data was obtained for this value of Λ. We also set the contact angle to 90° for all the results, since this simplifies the numerical implementation considerably. We note that in a previous study, very good agreement with experiments was found when using this value of contact angle in the simulations.[18] Furthermore, similar experiments reported in Ref. 10 show an equilibrium contact angle of 88°, very close to the value used here.

To present the considered model in a more general setting, we rewrite Eqs. (2) and (3) in a dimensionless form. We take the scales as $L = w = 100$ nm, and $T = 1$ ns, based on the typical in plane dimensions and the observed retraction times. We define the following dimensionless quantities:

$$\begin{aligned}
\mathbf{x}^* &= \frac{\mathbf{x}}{L}, & t^* &= \frac{t}{T}, \\
\rho^* &= \frac{\rho}{\rho_l}, & \mu^* &= \frac{\mu}{\mu_l}, \\
\mathbf{u}^* &= \frac{L}{T}\mathbf{u}, & p^* &= \frac{T}{\mu_l}p, \\
\kappa^* &= \kappa L, & \delta_s^* &= \delta_s L, \\
\mathrm{Re} &= \frac{\rho_l L^2}{\mu_l T}, & \mathrm{Ca} &= \frac{\mu_l L}{\sigma T}.
\end{aligned}$$

With these scales, our dimensionless equations are

$$\mathrm{Re}\,\rho^*\left(\partial_{t^*}\mathbf{u}^* + \mathbf{u}^*\cdot\nabla^*\mathbf{u}^*\right) = -\nabla^* p^* + \nabla^*\cdot\left(\mu^*\left(\nabla^*\mathbf{u}^* + \nabla^*\mathbf{u}^{*T}\right)\right) + \mathrm{Ca}^{-1}\kappa^*\delta_s^*\mathbf{n}, \tag{5}$$

$$\nabla^*\cdot\mathbf{u}^* = 0. \tag{6}$$

For our choice of parameters, the Reynolds number and capillary number are, respectively, $\mathrm{Re} \approx 16.8$, $\mathrm{Ca} \approx 0.26$, so the evolution takes place in a regime with a moderate dominance of inertial and surface tension effects over viscosity. The relevance of inertial effects, as well as the fact that contact angles involved are large, supports the use of the direct numerical modeling as described next.

We directly solve the N–S equations using a Volume of Fluid (VoF) based solver implemented in Gerris[27] and described in Ref. 28; we briefly survey the method here. Results obtained using Gerris are referred to as VoF results throughout this paper. The solution of the N–S equations is accomplished using a standard projection method. Spatial discretization is carried out using an adaptive octree; our adaptive mesh resolves the interface at a resolution of approximately 1 nm, and regions of high curvature are resolved to approximately 0.5 nm. The simulations that we present in Secs. III and IV are insensitive to any further refinements in the mesh. Gerris solves the N–S equations in two phases, and the VoF method tracks which fluid phase occupies a spatial point by introducing a volume fraction function $F(t, \mathbf{x})$, which gives the fraction of each computational cell

This article is copyrighted as indicated in the article. Reuse of AIP content is subject to the terms at: http://scitation.aip.org/termsconditions. Downloaded to IP: 128.235.83.176 On: Mon, 21 Sep 2015 16:48:41

occupied by the liquid phase. The volume fraction is advected with the velocity field according to the following equation:

$$\partial_t F + \mathbf{u} \cdot \nabla F = 0. \tag{7}$$

The VoF method naturally handles the breakup and coalescence of fluid regions, so that these phenomena do not require any separate treatment;[28,29] breakup is said to occur when a liquid region separates into two disconnected regions. The viscosity, μ, and density, ρ, depend on $F(t,\mathbf{x})$ by a mean of the respective liquid and ambient phase values. In order to minimize the effect of the ambient phase, we set $\mu_a = 0.01\mu_l$ and $\rho_a = 0.2\rho_l$. This choice of ρ_a is a compromise between minimizing the influence of the ambient phase and the computational cost of having very large differences between the ρ_l and ρ_a. The cell centered normal vector for the interface is given by approximating ∇F using a Mixed-Young's method[30] and the interface curvature is approximated using a modified height function method.[31–34] For all the computations, we only simulate a half of the period due to symmetry, so that $0 \le x \le \lambda_p/2$. Simulations with a computational domain of a full period were run for selected cases, and no difference was observed when compared with the half period simulations. In subsequent figures, we will often mirror the domain when we plot the simulations results, so that one or more periods are visible.

The partial wetting of Ni on the silicon dioxide (SiO_2) substrate is modeled by imposing a mirror condition on $F(t,\mathbf{x})$. Since the interface normal is given by ∇F, a mirror condition on the substrate implies that $\nabla F = (\partial_x F, 0, \partial_z F)$, and thus this is equivalent to a 90° contact angle. The limitation of imposing a 90° contact angle is not intrinsic to the VoF method,[31] however the numerical implementation of this contact angle is considerably simpler (and also arbitrary contact angles are not currently implemented in Gerris). Since the contact angle in the experiments[18] is very close (88°), the use of this simplification is well justified.

When a long strip of width $w = 100$ nm and height $h = 10$ nm is placed on a surface, it rapidly retracts to a half-cylinder, which we call a filament, of radius $r_0 = \sqrt{2wh/\pi} \approx 25$ nm; we remind the reader that this value of r_0 remains constant throughout this work, since it describes the radius of the half-cylinder corresponding to the central strip alone (without perturbation). Equation (1) therefore predicts that the critical wavelength of the central strip is approximately 160 nm. This result is consistent with the VoF simulations; we find that a half-cylindrical filament of radius r_0 is unstable when perturbed by a sinusoidal mode of a wavelength greater than approximately 160 nm, and stable otherwise. This result is insensitive to the slip length Λ; we tested the critical wavelength of such filaments with $\Lambda = 10$ nm, $\Lambda = 60$ nm, and a free slip boundary condition (equivalent to $\Lambda \to \infty$ limit and also to a standing jet) and found the critical wavelength to be the same to an accuracy of about 1%. We therefore use Eq. (1) to calculate the critical wavelength for filaments throughout this paper. While Eq. (1) strictly applies only to small perturbations, we will show below that at least in the present setting it also describes stability of sinusoidal perturbations, even if they are not small.

III. RESULTS

We first investigate the case $\lambda_p = 150$ nm; this value of λ_p is below the critical wavelength which is predicted by the R–P analysis for the central strip, $\lambda_c = 2\pi r_0 \approx 160$ nm. Fig. 3(a) (Multimedia view), shows the breakup of a rectangular-wave geometry for $A_p = 110$ nm and $w_p = 75$ nm. The cross section shows the pressure distribution in the liquid as it breaks up. The initially imposed shape quickly evolves, resulting in a low pressure region at the protrusion centers, $(x,z) = (n\lambda_p, 0)$ ($t = 0.5$ ns). As the protrusions retract, more liquid accumulates at the centers, while higher pressure necks form in between, $(x,z) = ((n+1/2)\lambda_p, 0)$ ($t = 1.0$ ns). While these necks have high negative curvature in the y-z plane, the pressure there is still high relative to the protrusion centers. Eventually, the resulting pressure gradient causes the necks to pinch off ($t = 1.5$ ns) and separate droplets form with a center to center spacing equal to λ_p ($t = 10$ ns).

We can contrast the described evolution with the one of a sinusoidal shape perturbation, with the same λ_p and total liquid volume. Figure 3(b) (Multimedia view), shows that the evolution initially follows a similar path: as the perturbations retract, low pressure regions again form at the

This article is copyrighted as indicated in the article. Reuse of AIP content is subject to the terms at: http://scitation.aip.org/termsconditions. Downloaded to IP: 128.235.83.176 On: Mon, 21 Sep 2015 16:48:41

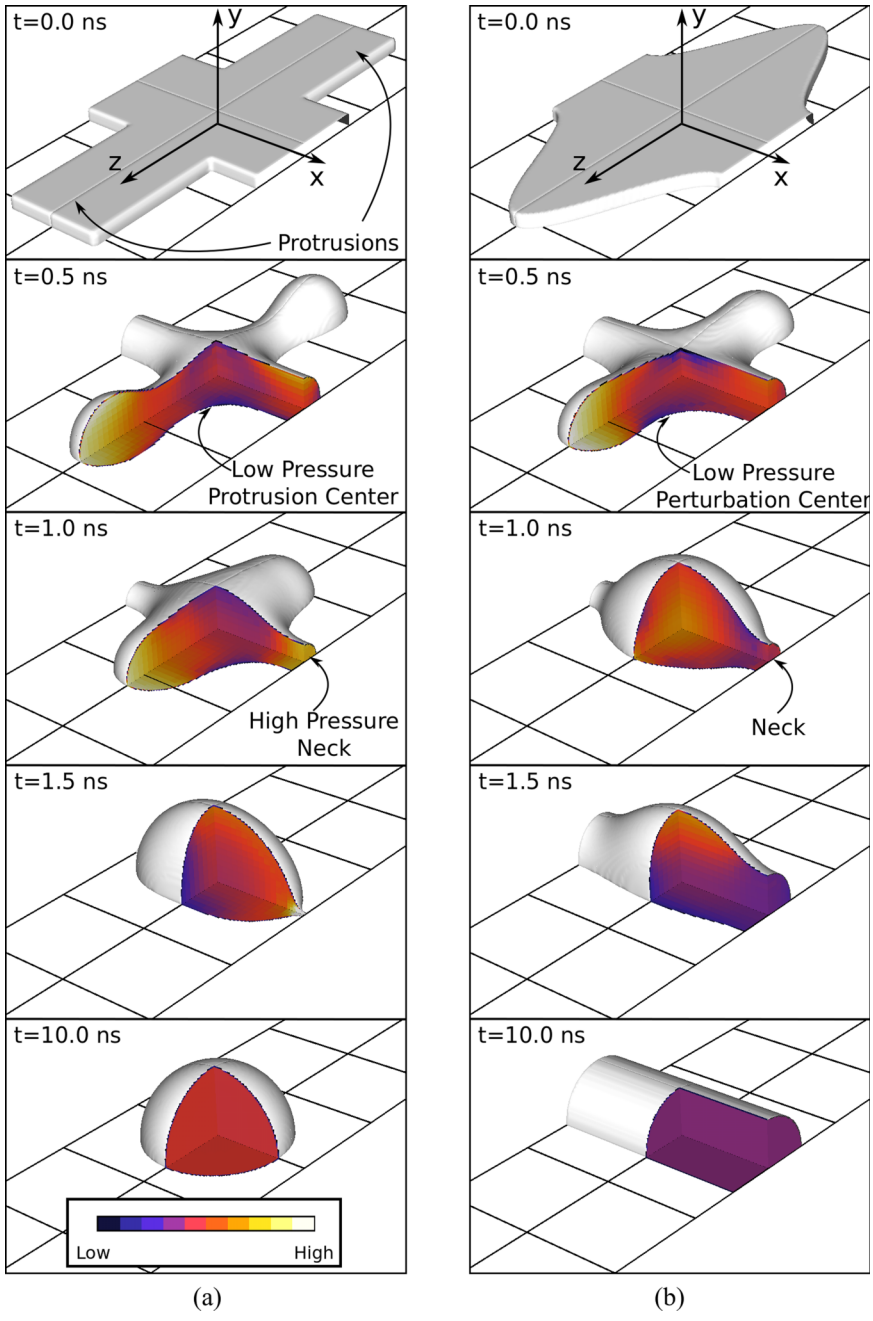

FIG. 3. Time evolution and the pressure distribution for the rectangular-wave and sinusoidal geometries with a perturbation wavelength of 150 nm: (a) rectangular-wave perturbed strip with $A_p = 110$ nm, $w_p = 75$ nm and (b) sinusoidally perturbed strip of the same volume as in (a) with $w_s = 100$ nm, $A_s = 110$ nm; see Fig. 1 for the definition of all geometric quantities. Each box is 75 nm by 75 nm, and the pressure scale is the same for both figures. (Multimedia view) [URL: http://dx.doi.org/10.1063/1.4931086.1] [URL: http://dx.doi.org/10.1063/1.4931086.2]

perturbation centers $(x, z) = (n\lambda_s, 0)$. After this initial stage, however, the evolution is different from the rectangular-wave geometry. Most notably, the peaks of sinusoidal perturbations retract much more quickly, and nearly all of the liquid accumulates close to the perturbation centers. While negative curvature necks still form in between, the pressure in these necks is actually lower than in the centers ($t = 1.0$ ns), contrary to what is found for rectangular-wave geometry. Consequently, the structure stabilizes ($t = 1.5$ ns), ultimately forming a half-cylindrical filament ($t = 10.0$ ns).

This article is copyrighted as indicated in the article. Reuse of AIP content is subject to the terms at: http://scitation.aip.org/termsconditions. Downloaded to IP: 128.235.83.176 On: Mon, 21 Sep 2015 16:48:41

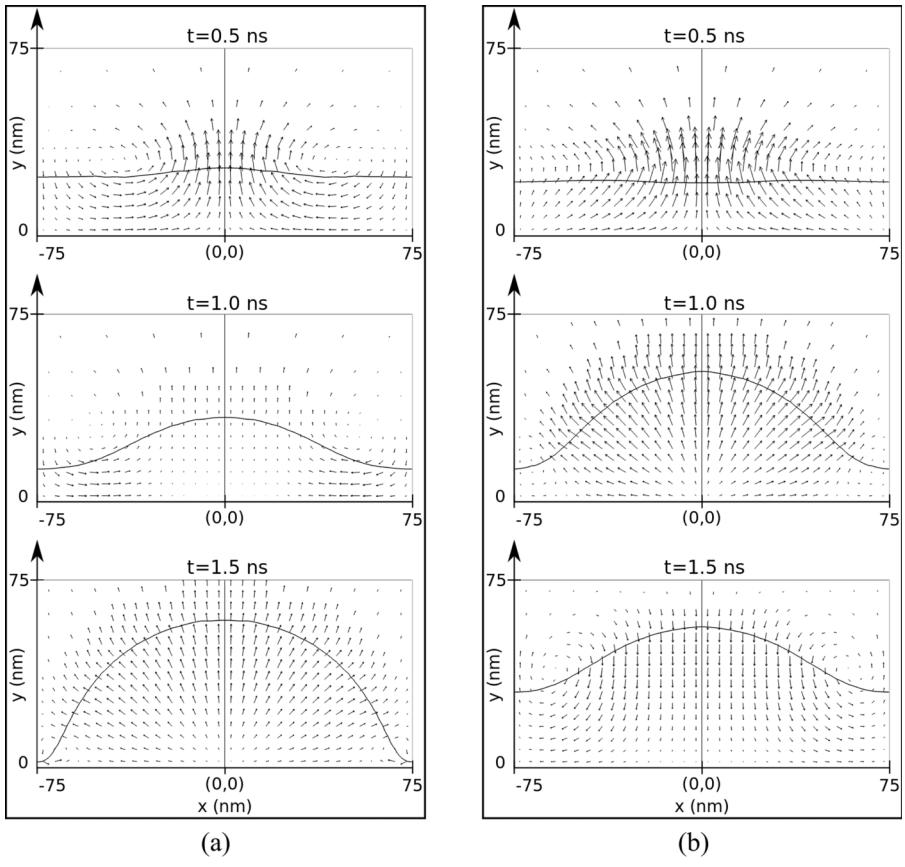

FIG. 4. Time evolution of the velocity field in the $z = 0$ plane for times $t = 0.5$, 1.0, and 1.5 ns, for (a) the rectangular-wave and (b) sinusoidal geometries. The respective parameters are the same as in Fig. 3. The solid curve shows the interface. The arrows show the velocity in both the liquid and ambient phases.

Figure 4 shows the velocity field of each geometry from Fig. 3 in the $z = 0$ plane, for $x \in (-\lambda_p/2, \lambda_p/2)$, where again $\lambda_p = 150$ nm. For the rectangular-wave geometry (Fig. 4(a)), at $t = 0.5$ ns, vortices have developed at the interface approximately midway between the origin and the necks, draining the liquid from the necks to the low pressure region at $x = 0$. This trend continues for longer times, with the vortices slowly moving towards the necks, draining the liquid from there and leading eventually to rupture. Meanwhile, for the sinusoidal geometry, shown in Fig. 4(b), the vortices form later and show a much weaker component of flow towards $x = 0$ and are therefore not strong enough to lead to breakup.

In addition to the rectangular waveform perturbation, we have considered the breakup of other initial configurations that we mention here only briefly. We find that triangle waveform patterns (with a base attached to the central filament) break up similarly to sinusoidal type geometries and so do not display the richness of behavior as the rectangular waveform perturbation. If a vertex of a triangular perturbation is connected to a filament, a breakup occurs at the vertex, without influencing stability of the filament. Therefore, it appears that a rectangular waveform perturbation is the most obvious one if the goal is to modify the stability properties of the central filament.

Next, we consider the evolution of the rectangular-wave geometry when varying the size of the protrusions. Figure 5 shows the structures characterized by the same dimensions as in Fig. 3, except that in Fig. 5(a), $A_p = 100$ nm, and in Fig. 5(b), $A_p = 300$ nm (Multimedia view). When A_p is too small, the structure does not break up, meaning that there is a critical amplitude, A_c, below which breakup does not occur. For small A_p, the protrusions collapse too quickly, so that the low pressure region in the junction is not sustained long enough for breakup to occur. The existence of A_c is consistent with the R–P stability predictions, since for sufficiently small A_p, linear stability should

This article is copyrighted as indicated in the article. Reuse of AIP content is subject to the terms at: http://scitation.aip.org/termsconditions. Downloaded to IP: 128.235.83.176 On: Mon, 21 Sep 2015 16:48:41

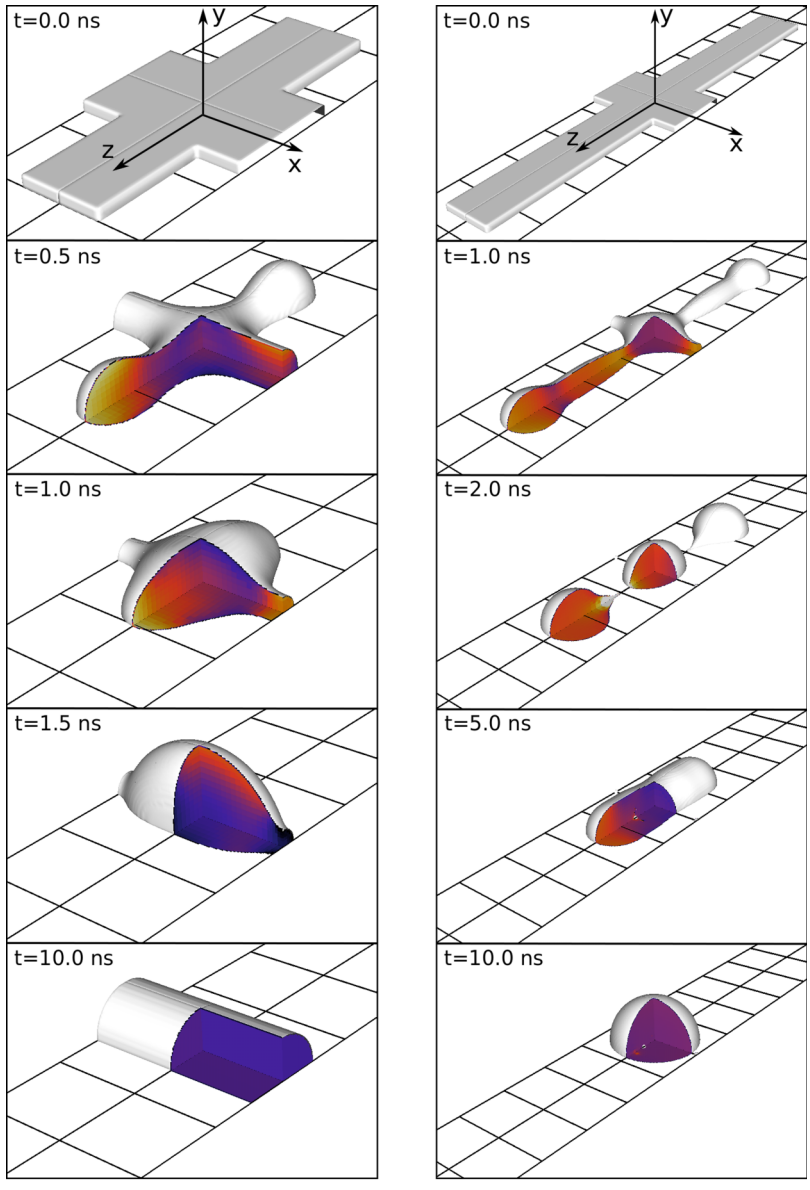

FIG. 5. Time evolution and the pressure distribution for $\lambda_p = 150$ nm, $w_p = 75$ nm, showing a stable case and a case with secondary protrusion breakup: (a) $A_p = 100$ nm, and (b) $A_p = 300$ nm. Each box is 75 nm by 75 nm, and the pressure scale is the same as in Fig. 3. (Multimedia view) [URL: http://dx.doi.org/10.1063/1.4931086.3] [URL: http://dx.doi.org/10.1063/1.4931086.4]

hold independently of the perturbation shape. On the other hand, when A_p is sufficiently large, a secondary breakup occurs, such that the protrusions form separate side-droplets that then recoalesce to form central droplets at $x = n\lambda_p$. A similar situation is observed in experiments.[18] We note (and discuss further below) that for very large A_p, a set of side droplets form as the droplets do not re-coalesce, similar to the two-dimensional array of end droplets shown in Figs. 2(h) and 2(j). A more complete discussion of possible breakup mechanisms is given next; as we will see, there is still a more diverse range of end states to be described. For now, it is important to emphasize the most interesting point: although perturbations add to the total volume and may therefore be expected to stabilize short wavelengths, their influence may be opposite, leading actually to *instability* at perturbation wavelengths that would be expected to be stable based on the classical R–P prediction.

This article is copyrighted as indicated in the article. Reuse of AIP content is subject to the terms at: http://scitation.aip.org/termsconditions. Downloaded to IP: 128.235.83.176 On: Mon, 21 Sep 2015 16:48:41

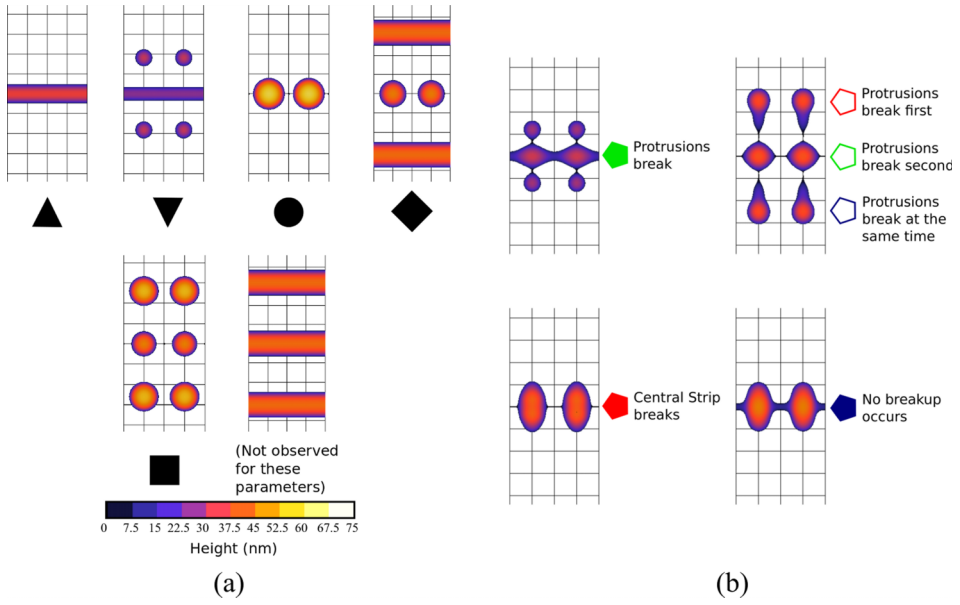

FIG. 6. (a) Classification of end states resulting from the evolution of the rectangular-wave geometry defined in Fig. 1(b). Each symbol below a sketch of a possible end state is used in Figs. 7-10 to show that this particular end state is observed. The end state consisting of three parallel filaments is not observed for the parameters considered and is included for completeness. (b) Classification of dynamics. Filled symbols show the cases when either the protrusion breaks, the central strip breaks, or no breakup occurs at any time, and the color of each indicates which of these cases is observed. Hollow symbols show cases when both the central strip and the protrusions of the rectangular-wave breakup, and the color shows the order of the breakup scenarios.

A. Parametric dependence

In this section, we explore the dependence of the dynamics on the parameters A_p, w_p, and λ_p. To reduce the number of parameters, unless otherwise noted, we fix $w = 100$ nm and $h = 10$ nm.

Figure 6 classifies the dependence of the breakup process on w_p and A_p for two wavelengths, λ_p. Figure 6(a) shows the observed end configurations. As shown, a diverse range of end states can be achieved by harnessing this initial geometry. The one-dimensional arrays (circle) and arrays with side droplets (square), as also observed in Ref. 18, viz., Fig. 2, are accompanied by additional configurations such as a filament (triangle), a filament with side droplets (inverted triangle), and a one-dimensional array with side filaments (diamond). Although not observed for these parameters, a sixth state, consisting of three parallel filaments, is also possible. We note that within the considered framework, any resulting filaments ultimately should destabilize due to the R–P instability mechanism, and an array of droplets should form with a distribution according to the prediction of the R–P analysis as discussed in Ref. 11. However, this subsequent breakup takes place significantly later than the formation of the filament; Eq. (1) suggests that a filament resulting from, say, $A_p = 110$ nm, $\lambda_p = 150$ nm, $w_p = 75$ nm, would take nearly twice as long to break up when compared to the time the filament would take to form (4.5 versus 2 ns). This longer time evolution is not considered in the present work; we note that in the context of liquid metal films that are in liquid state for a short time, any state discussed here may as well be the final outcome.

Figure 6(b) shows the relevant dynamics of the breakup; our goal is to classify what type of breakup occurs, during any point in the evolution of the structure, even if later on, there is recoalescence. We classify the evolution of this system according to whether the protrusions and/or the central strip break up, and the order in which the breakup occurs. Hollow symbols show that both the protrusion and the central strip rupture, and the color corresponds to whether the protrusions break off before the central strip ruptures (red (dark grey) symbols), after the central strip ruptures (green (light grey) symbols), or at approximately the same time as the central strip ruptures (blue (black) symbols). All other cases are shown using filled symbols: blue (black) indicates that no

This article is copyrighted as indicated in the article. Reuse of AIP content is subject to the terms at: http://scitation.aip.org/termsconditions. Downloaded to IP: 128.235.83.176 On: Mon, 21 Sep 2015 16:48:41

breakup occurs at any time during the evolution, red (dark grey) that only the protrusions break off, and green (light grey) that only the central strip ruptures. These breakup scenarios may be followed by a secondary recoalescence of droplets to produce the static states discussed above. The end state is not independent of the dynamics, for example, when the end state includes side droplets and side filaments, indicated by an inverted triangle, a square, and a diamond in Fig. 6(a), this must be accompanied by the protrusions breaking off (filled green (light grey), hollow red (dark grey), hollow green (light grey), and hollow blue (black) symbols in Fig. 6). We find that decoupling the classification of the end states and dynamics will more effectively facilitate discussion of the parametric dependence.

Figure 7(a) summarizes the possible static and dynamic states for $\lambda_p = 150$ nm. Let us first consider an intermediate range of w_p for which a breakup occurs, i.e., 45 nm $\lesssim w_p \lesssim$ 75 nm. Within this range, we find that there is a critical amplitude, A_c, below which there will be no breakup and the end state is a filament, and above which the central strip will rupture at some point. We find that A_c is about 110 nm for $w_p \gtrsim 75$ nm, and it increases to between 150 and 200 nm for 45 nm $\lesssim w_p \lesssim 65$ nm. However, for $A_p > A_c$, variation of A_p has no effect on the stability of the central strip. That is, once A_p is sufficiently large, any further increase does not affect whether or not the central strip breaks up at some point in time. For w_p between 65 nm and 95 nm, side droplets form when $A_p = 500$ nm; for small w_p (25 nm $\lesssim w_p \lesssim$ 45 nm), side droplets form for $A_p \approx 300$ nm, although the strip does not rupture for $w_p = 25$ nm. For large A_p, if side droplets do not form, the protrusions introduce a large amount of excess liquid which may prevent the formation of a central array, even though the central strip does break up (see, for example, $w_p = 95$ nm, $A_p = 200$ nm, and 300 nm).

The stability of the central strip is also affected by the protrusion width, w_p. For small w_p, such as 25 nm, shown in Fig. 7(a), the central filament remains stable for all values of A_p, and the protrusions may either not break at all for small A_p (e.g., 100 nm), break off and coalesce for larger A_p (≈150 nm), or break off and remain separated for even larger values of A_p (≳200). Larger w_p (≳45 nm) is associated with a critical protrusion amplitude, A_c, as discussed above. It is interesting to note that for $w_p = 45$ nm and $A_p \gtrsim 200$ nm, the protrusion breaks off first, yet the central strip still ruptures. This may seem counterintuitive, as the protrusions drive the breakup of the central

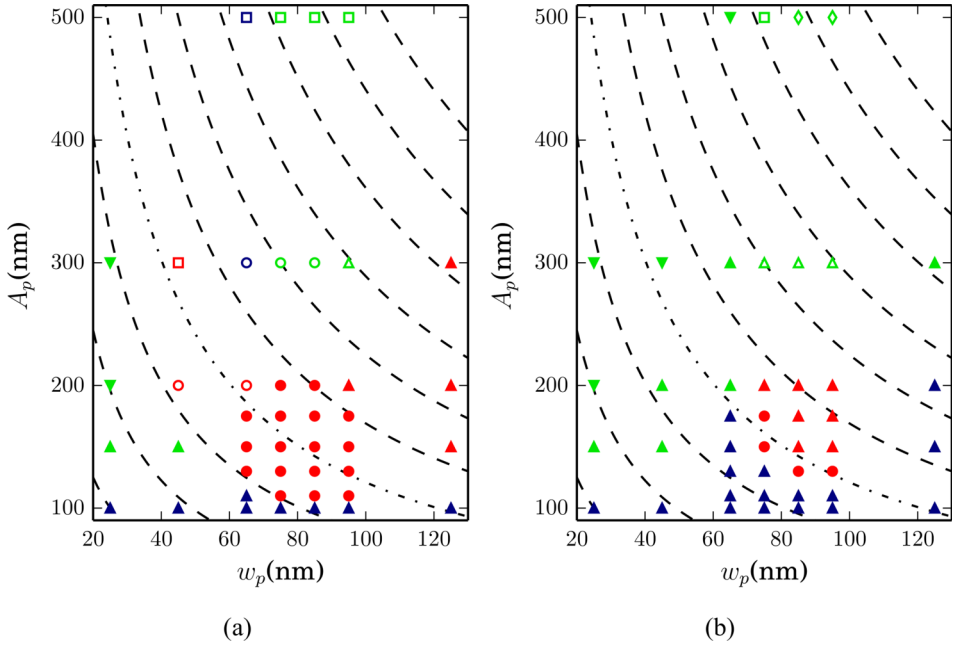

FIG. 7. Phase plots classifying the dynamics and end states for the evolution of the geometry shown in Fig. 1(b), for two values of λ_p. The symbols shape gives the end state produced by the breakup (Fig. 6(a)), while the symbol color classifies the dynamics (Fig. 6(b)). (a) $\lambda_p = 150$ nm and (b) $\lambda_p = 130$ nm. The dashed curves show constant effective cross-sectional area, Ω_{eff}. The area increases from bottom left to top right.

This article is copyrighted as indicated in the article. Reuse of AIP content is subject to the terms at: http://scitation.aip.org/termsconditions. Downloaded to IP: 128.235.83.176 On: Mon, 21 Sep 2015 16:48:41

strip. However, in these cases, the time at which the protrusions break is comparable to the time when the central strip breaks, indicating that a sufficiently large perturbation is still imparted to the strip that breakup could occur even in the absence of the protrusion. For very large w_p, such as $w_p = 125$ nm, the central filament remains stable; for $A_p = 300$ nm, the protrusions break off from the filament at some point of the evolution but eventually recoalesce.

Figure 7(b) shows the corresponding results for $\lambda_p = 130$ nm. For this smaller λ_p, a much narrower range of parameters allows for the formation of arrays of droplets. Instead, we most often find either a filament or a filament with side droplets. To explain this, first note that for the same value of A_p and w_p, there is a larger effective area, Ω_{eff}, for $\lambda_p = 130$ nm than for $\lambda_p = 150$ nm. Larger Ω_{eff} implies that any droplets resulting from breakup will not only be more closely spaced due to the smaller value of λ_p but also larger in radius, which will tend to lead to recoalescence. Second, as the structure begins its retraction, smaller λ_p implies a larger negative curvature in the x-z plane at $x = (n + 1/2)\lambda_p$, which will tend to stabilize the structure. When the central strip does rupture at some point during the retraction, increasing A_p to 500 nm, for large enough w_p, leads to the unique case of a one-dimensional array of droplets with side filaments on either side, as the large amount of liquid and narrower spacing leads to the coalescence of the side droplets produced by the protrusions breaking off. We note that in addition to $\lambda_p = 130$ nm, we also considered $\lambda_p = 110$ nm, but for such a small λ we did not find breakup of the central strip for any combination of protrusion parameters. Also, geometries characterized by larger values of λ_p are considered numerically and experimentally in Ref. 18; droplets resulting from the breakup of large λ_p geometries tend not to recoalesce, leading to arrays of droplets with spacing exactly equal to λ_p, and as λ_p is increased further, further droplets may form leading to arrays with spacing of $\lambda_p/2$ or smaller.

Finally, we briefly consider the effects of slip length, Λ, on the results. We consider the effect of Λ only for $w_p = 75$ nm and $\lambda_p = 150$ nm, while permitting A_p to vary; this parameter set is sufficient to demonstrate the main effects of slip on the dynamics of breakup. Figure 8 shows three important consequences of slip on both the dynamic and static states. First, for small A_p ($\lesssim$200 nm), smaller Λ promotes breakup of the central strip; this is due to the fact that, in order for the central

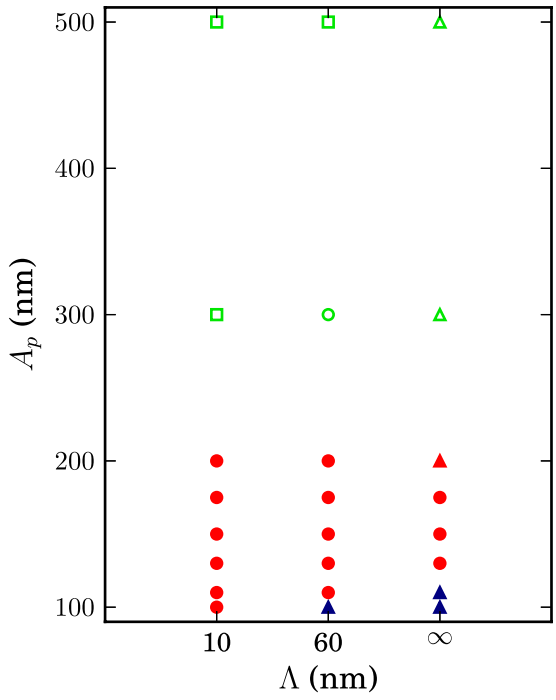

FIG. 8. Parametric dependence on the slip length Λ for $\Lambda = 10$ nm, 60 nm, and ∞ (free slip condition). Symbols and colors indicate the same static states and dynamics as in Fig. 6. The parameters λ_p and w_p are fixed at 150 nm and 75 nm, respectively.

This article is copyrighted as indicated in the article. Reuse of AIP content is subject to the terms at: http://scitation.aip.org/termsconditions. Downloaded to IP: 128.235.83.176 On: Mon, 21 Sep 2015 16:48:41

strip to break up, the protrusion must not collapse too quickly, so that a smaller slip delays the collapse of the protrusion and allows breakup. Thus, the critical amplitude above which breakup occurs, A_c, increases with Λ. Second, for large A_p ($\gtrsim$300), small Λ prevents recoalescence of the side droplets with the liquid near $z = 0$, so that an array with side droplets is possible for smaller A_p, as indicated by the square symbols (compare $\Lambda = 10$ nm to $\Lambda = 60$ nm). Finally, large Λ facilitates recoalescence of droplets; for the free slip case, note that even when rupture of the central strip occurs, the droplets inevitably recoalesce when $A_p > 175$ nm.

IV. DISCUSSION

A. Relation to Rayleigh-Plateau instability mechanism

One important finding so far is that the chosen rectangular-wave geometry leads to the formation of droplets characterized by a spacing that is appreciably smaller than the critical wavelength expected from the prediction of the R–P instability analysis. This holds true even if only the cross-sectional area of the central strip, Ω_0, is considered: of course, if the total area (including protrusions), Ω_{eff}, is used, the result leads to even higher efficiency when compared to the R–P prediction. To be specific, the central strip considered so far has a critical R–P wavelength of $\lambda_c(\Omega_0) \approx 160$ nm, and our simulation results find droplet formation for $\lambda_p = 130$ and 150 nm. In particular, for $\lambda_p = 150$ nm, parameters leading to the formation of a one-dimensional array of droplets (indicated by a circle in Fig. 7) show $\lambda_c(\Omega_{\text{eff}})$ to be 1.5-2 times larger than λ_p.

B. Role of the effective area

Recall Fig. 7, where we plot dashed curves showing constant Ω_{eff}. Consider first $\lambda_p = 150$ nm, plotted in Fig. 7(a). For relatively small Ω_{eff}, (indicated by lines in the lower left corner), it is impossible to destabilize a strip, as either the protrusions must be so thin (small w_p) that they break off without destabilizing effect, or A_p is below the critical value. In the other extreme, for large Ω_{eff} (top right corner), either A_p must be so large that side droplets form or w_p must be so large that no breakup occurs. Thus, only strips with an intermediate range of Ω_{eff} result in one-dimensional arrays of droplets. We also note that differing parameters lead to a variety of results for the same Ω_{eff}. Consider the line of constant Ω_{eff} passing near $w_p = 45$ nm and $A_p = 300$ nm (plotted as a dashed-dotted line in Fig. 7(a)). Large amplitude perturbations permit the formation of a two-dimensional array, as indicated by a square. Moving rightwards along the line, decreasing A_p results in a one-dimensional array (see, e.g., $w_p = 75$ nm and $A_p = 175$ nm), while further reduction in A_p leads to an end state which is a filament (see, e.g., $w_p = 125$ nm and $A_p = 100$ nm).

Figure 7(b) shows the corresponding results for $\lambda_p = 130$ nm. Similarly to Fig. 7(a), perturbations of strips with small Ω_{eff} (lower left corner) do not lead to the formation of an array of droplets, while perturbations of strips with large Ω_{eff} (upper right corner) result in either a filament or an array of droplets with side filaments. Only strips with an intermediate range of Ω_{eff} result in one- and two-dimensional arrays. Just as in the $\lambda_p = 150$ nm case, the end state for the same Ω_{eff} depends on the choice of A_p and w_p. To show this, consider the line passing near $w_p = 65$ nm and $A_p = 175$ nm (plotted as a dashed-dotted line); we see that only a small range of parameters permits the formation of an array of droplets. For larger w_p, breakup of the central strip still occurs, but these droplets subsequently recoalesce. Thus, for both $\lambda_p = 130$ nm and 150 nm, Ω_{eff} does not determine the end state, as varying w_p and A_p can completely change both the type of breakup that occurs, as well as whether or not recoalescence occurs after any breakup.

Next, we discuss the effect of λ_p on the breakup. Figure 9 shows (λ_p, w_p) phase diagram for a fixed $A_p = 150$ nm, with curves of constant effective areas, Ω_{eff}. This plot shows that larger λ_p perturbations tend to promote breakup. This holds when moving along lines of constant Ω_{eff} from $w_p = 75$ nm and $\lambda_p = 150$ nm, which results in a one-dimensional array of droplets, to $w_p = 65$ nm and $\lambda_p = 130$ nm, where no breakup occurs at all. Similarly, perturbed strips with Ω_{eff} that breakup for $\lambda_p = 130$ nm (red (dark grey) symbols) do not break up for $\lambda_p = 120$ nm (blue (black) symbols). As noted above, small Ω_{eff} results in strips that do not break up, so that no breakup occurs for

This article is copyrighted as indicated in the article. Reuse of AIP content is subject to the terms at: http://scitation.aip.org/termsconditions. Downloaded to IP: 128.235.83.176 On: Mon, 21 Sep 2015 16:48:41

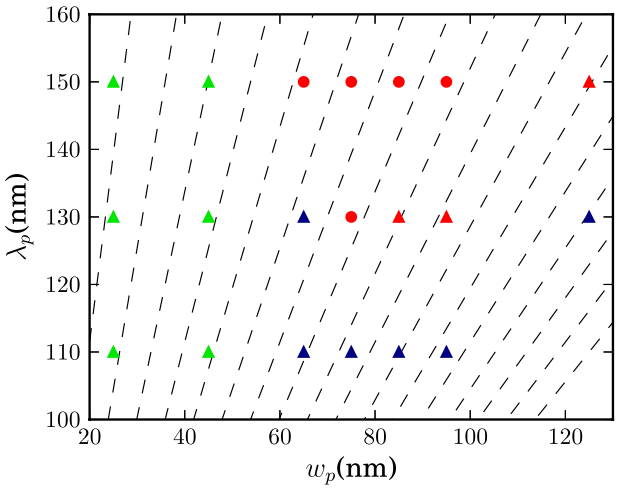

FIG. 9. Parametric dependence on λ_P and w_P for $A_P = 150$ nm. Symbols and colors indicate the same end states and dynamics as in Fig. 7. Dashed lines show curves of constant effective cross sectional area, Ω_{eff}. The area increases from bottom right to top left.

$\lambda_p = 130$ nm, and $w_p \leq 65$ nm. It is worth noting here that λ_p has little effect on the behavior of the protrusions when w_p is fixed. For $w_p \leq 45$ nm, Fig. 9 shows that for all λ_p, the protrusions break off, as indicated by the green (light grey) color. On the other hand, for $w_p \geq 65$ nm, the protrusions do not break off, as indicated by the red (dark grey) and blue (black) colors.

C. Summary of the breakup

We are now in a position to summarize the mechanism by which the rectangular-wave geometry breaks up. The primary driving mechanism of the break up is based on the fact that the cross-shaped geometry near $x = n\lambda_p$ leads to an initial negative x-z curvature, which, as the structure begins its initial retraction, results in the formation of a low pressure bulge. Along the central strip, near $x = (n + 1/2)\lambda_p$, the liquid retracts to a half-cylinder. A positive x-y curvature of magnitude $1/\sqrt{2hw/\pi}$ leads to a large corresponding Laplace pressure at $x = (n + 1/2)\lambda_p$ between two low pressure bulges at $x = n\lambda_p$, and so liquid drains out of the neck into the bulges, leading to breakup.

Figures 7(a) and 7(b) show that neither the end state nor the dynamics are entirely determined by the effective area Ω_{eff}. For strips with a small Ω_{eff}, either the perturbation has a small A_p and it cannot break the strip up or w_p is so small that the protrusions form side droplets, and the strip still does not break up. Strips with large Ω_{eff} may breakup, and then either a two-dimensional array forms, or the droplets will recoalesce into a filament. Only for strips with an intermediate range of Ω_{eff} is a one-dimensional array of droplets a possible end state.

Since the dynamics of the retraction may vary with the same Ω_{eff} and changing the amount of liquid per wavelength necessarily changes the possible end states, it is necessary to consider any breakup in terms of the dynamics (classification shown by color in Figs. 7(a) and 7(b)). The amplitude A_p is only important in that it must be larger than a critical one, A_c, in order for the central strip to break up. For larger values of A_p and a fixed w_p, the central strip does not change its dynamics; that is, once breakup is possible, any further increase in A_p does not affect whether or not the central strip breaks up at some point in time.

Whenever droplets form, it is found that the resulting center to center spacing is always equal to λ_p, and as discussed in Sec. IV A, λ_p is generally smaller than the smallest possible spacing that can be understood using the R–P instability analysis. Thus, a rectangular-wave edge perturbation is a highly effective way of generating arrays of closely spaced droplets, far below what is expected

This article is copyrighted as indicated in the article. Reuse of AIP content is subject to the terms at: http://scitation.aip.org/termsconditions. Downloaded to IP: 128.235.83.176 On: Mon, 21 Sep 2015 16:48:41

based on the R–P instability mechanism. We note that the aspect ratio of the perturbations is important: even if λ_p and Ω_{eff} are specified, one of w_p or A_p is still a free parameter; selected value can strongly influence the end state.

D. Formation of satellite droplets

The end state for a variety of parameters for $\lambda_p = 150$ nm includes small satellite droplets between the droplets in the central array; no satellite droplets are present in the end state when $\lambda_p = 130$ nm. Figure 10(a) shows the snapshots of the droplet, for $A_p = 150$ nm, $\lambda_p = 150$ nm,

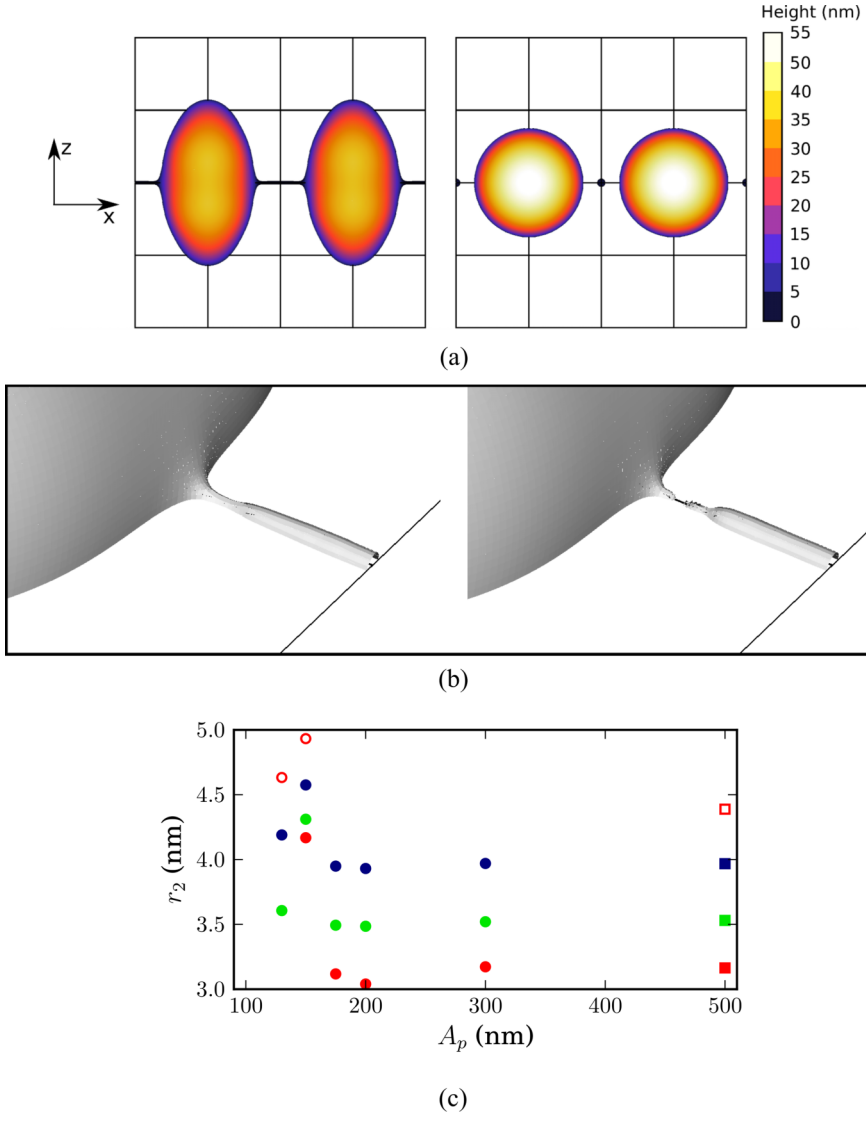

FIG. 10. (a) Satellite droplets for $w_p = 75$ nm and $A_p = 150$ nm. One box is 75 nm by 75 nm. (b) Close up of the breakup of the filament connecting primary droplets for $w_p = 75$ nm and $A_p = 150$ nm. A mirror condition is applied at the solid black line, so that the figure shows half of the filament. Note that an instability appears to be developing after the breakup of the thin filament connecting the two main droplets, leading possibly to the formation of tertiary droplets. Capturing the details of this breakup would require higher resolution than used in the present study (note insufficient grid resolution resulting in non-smooth surface of the connecting filaments). (c) Satellite droplet radius for $w_p = 65$ nm (red (dark grey)), $w_p = 75$ nm (green (light grey)), $w_p = 85$ nm (blue (black)), and $w_p = 95$ nm (hollow red (dark grey)). Circles indicate that the equilibrium is a one-dimensional array, and squares indicate that the end state is an array with side droplets. For these results, $\lambda_p = 150$ nm.

This article is copyrighted as indicated in the article. Reuse of AIP content is subject to the terms at: http://scitation.aip.org/termsconditions. Downloaded to IP: 128.235.83.176 On: Mon, 21 Sep 2015 16:48:41

and $w_p = 75$ nm, just prior to breakup (left), and at the end state (right). Prior to the breakup, a very thin filament connects the two droplets; after the breakup, there are small satellite droplets located at $x = (n + 1/2)\lambda_p$. The formation of these satellite droplets is due to the fact that the thin filament breaks up near its ends. Figure 10(b) shows a closeup of the connecting filament just prior to (left) and after (right) the breakup. Just prior to the breakup, the connecting filament begins to neck at a point close to the primary droplet, which results in the filament breaking up near its ends. After breakup, this filament retracts into a small satellite droplet. The size of the satellite droplet is therefore determined by the amount of liquid in the connecting filament. Figure 10(c) shows the radius of the satellite droplets for all parameters when the central strip breaks up and a satellite droplet results, for $\lambda_p = 150$ nm. In general, larger w_p leads to larger satellite droplets. Regarding the influence of A_p, we find that the size of the satellite droplet peaks for $A_p = 150$ nm and is approximately the same for larger values of A_p. We generally find that A_p and w_p influence the formation of different length filaments and consequently the formation of satellite droplets of different sizes. We note, however, that the size of satellite droplets depend on the nature of the evolution in a complicated manner, whether protrusions break up or not, and/or when they break up. We leave the investigation of this issue for future work.

V. CONCLUSIONS

In this paper, we show that the initial geometry of a liquid deposited on a substrate has a strong influence on the morphology of the final patterns that result due to the liquid instability. In particular, we find that appropriate choices of the initial geometry may lead to instabilities even in configurations that are expected to be stable based on the analogy with the R–P instability mechanism. Our computational results show that the initial liquid shape strongly influences the distribution of the pressure in the liquid. Therefore, rectangular waveform perturbations, considered in this work, lead to evolution that is considerably different from, for example, the one resulting if sinusoidal waveform perturbations are applied.

While the methods that we use are of general validity, we concentrate particularly on recent experiments carried out with liquid metals on nano-scale, where the ability to control the location and size distribution of the resulting nano-particles is of fundamental interest in applications in the field of nano-assembly. We show that a diverse range of nano-particle arrays can be observed and that the rectangular-wave geometries perturbed by short wavelengths (shorter than the critical wavelength predicted by the R–P instability) exhibit a complex nonlinear evolution. We classify the dynamic behavior as well as the end states for the perturbations that differ by their aspect ratio and the perturbation wavelengths, λ_p. We demonstrate that it is possible to produce arrays of droplets with the spacing, λ_p, as small as half the critical wavelength predicted by the R–P instability mechanism. Added complexity is introduced by the fact that the aspect ratio of the introduced perturbations plays an important role: for example, given an "effective" area, Ω_{eff} (total volume of the liquid per λ_p), a significantly different evolution can be observed for different aspect ratios. Depending on the parameters, one-dimensional arrays of droplets for an intermediate range of Ω_{eff} can then be obtained; larger Ω_{eff} tends to produce central arrays of droplets with droplet arrays on the sides (two-dimensional arrays), while smaller Ω_{eff} structures do not break up. Additional configurations are possible as well, see Fig. 6 for a complete classification.

One particular feature of the instabilities that are observed in this work is the complex coupling between the dynamics and end configurations, with differing dynamics leading to possibly the same end states, as illustrated in Fig. 6. Our study demonstrates some, perhaps not obvious, features of the instability development. For example, we find that the perturbation amplitude, A_p, in general has to be larger than a critical value, A_c, for breakup to occur, and for some cases, increasing A_p results in the final state transitioning from a filament, to a one-dimensional array, back to a filament, and into a two-dimensional array of droplets. Decreasing λ_p tends to prevent the formation of droplets, and for a very small λ_p, the central strip does not rupture at all. The slip length, Λ, is found to have a significant effect on the formation of arrays and the stability of the structures, with a smaller Λ associated with breakup and the formation of arrays, and a larger Λ either preventing the breakup

This article is copyrighted as indicated in the article. Reuse of AIP content is subject to the terms at: http://scitation.aip.org/termsconditions. Downloaded to IP: 128.235.83.176 On: Mon, 21 Sep 2015 16:48:41

altogether or leading to recoalescence of the resulting droplets after the breakup occurs. Therefore, by varying the geometry and slip, it is possible to obtain, in a controllable manner, a large range of different dynamics and a variety of end states.

In the present work, we have focused on the influence of liquid geometry on the evolution and have not considered variation of material parameters that may lead to transition between inertial, viscous, and capillarity dominated regimes. Other interesting considerations could include (i) the role of surface active contaminants, as metals are subject to adsorption of species that lower their tension, and (ii) the role of heat transfer between the metal and the substrate leading to variation of material parameters and additional effects including thermo-capillary ones. We leave such studies for a future work and note that ongoing work in material science makes them highly relevant.

ACKNOWLEDGMENTS

The authors acknowledge many useful discussions with J. Diez, J. Fowlkes, A. Gonzalez, P. D. Rack, N. Roberts, and Y. Wu. This work was partially supported by the NSF Grant Nos. CBET-1235710 and DMS-1320037.

[1] G. Fleming and M. Ratner, "Grand challenges in basic energy sciences," Phys. Today **61**(7), 28 (2008).
[2] S. Henley, J. Carey, and S. Silva, "Metal nanoparticle production by pulsed laser nanostructuring of thin metal films," Appl. Surf. Sci. **253**, 8080 (2007).
[3] S. Fan, M. Chapline, N. Franklin, T. Tombler, A. Cassell, and H. Dai, "Self-oriented regular arrays of carbon nanotubes and their field emission properties," Science **283**, 512 (1999).
[4] S. Maier, P. Kik, H. Atwater, S. Meltzer, E. Harel, B. Koel, and A. Requicha, "Local detection of electromagnetic energy transport below the diffraction limit in metal nanoparticle plasmon waveguide," Nat. Mater. **2**, 229 (2003).
[5] S. Sun, C. Murray, D. Weller, L. Folks, and A. Moser, "Monodisperse FePt nanoparticles and ferromagnetic FePt nanocrystal superlattices," Science **287**, 1989 (2000).
[6] S. Maier, *Plasmonics: Fundamentals and Applications* (Springer-Verlag, New York, 2007).
[7] S. Baderi, "Colloquium: Opportunities in nanomagnetism," Rev. Mod. Phys. **78**, 1 (2006).
[8] Y. Min, M. Akbulut, K. Kristiansen, Y. Golan, and J. Israelachvili, "The role of interparticle and external forces in nanoparticle assembly," Nat. Mater. **7**, 527 (2008).
[9] J. Fowlkes, N. Roberts, Y. Wu, J. Diez, A. González, C. Hartnett, K. Mahady, S. Afkhami, L. Kondic, and P. Rack, "Hierarchical nanoparticle ensembles synthesized by liquid phase directed self–assembly," Nano Lett. **14**, 774 (2014).
[10] J. Fowlkes, L. Kondic, J. Diez, Y. Wu, and P. Rack, "Self-Assembly versus directed assembly of nanoparticles via pulsed laser induced dewetting of patterned metal films," Nano Lett. **11**, 2478 (2011).
[11] L. Kondic, J. Diez, P. Rack, Y. Guan, and J. Fowlkes, "Nanoparticle assembly via the dewetting of patterned thin metal lines: Understanding the instability mechanisms," Phys. Rev. E **79**, 026302 (2009).
[12] L. Rayleigh, "On the instability of jets," Proc. London Math. Soc. **1**, 4 (1878).
[13] J. Eggers, "Nonlinear dynamics and breakup of free-surface flows," Rev. Mod. Phys. **69**, 865 (1997).
[14] T. Driessen, R. Jeurissen, H. Wijshoff, F. Toschi, and D. Lohse, "Stability of viscous long liquid filaments," Phys. Fluids **25**, 062109 (2013).
[15] F. Brochard-Wyart and C. Redon, "Dynamics of liquid rim instabilities," Langmuir **8**, 2324 (1992).
[16] S. Davis, "Moving contact lines and rivulet instabilities. Part 1. The static rivulet," J. Fluid Mech. **98**, 225 (1980).
[17] J. Diez, A. Gonzalez, and L. Kondic, "On the breakup of fluid rivulets," Phys. Fluids **21**, 082105 (2009).
[18] N. Roberts, J. Fowlkes, K. Mahady, S. Afkhami, L. Kondic, and P. Rack, "Directed assembly of one- and two-dimensional nanoparticle arrays from pulsed laser induced dewetting of square waveforms," ACS Appl. Mater. Interfaces **5**, 4450 (2013).
[19] Z. Nie, A. Petukhova, and E. Kumacheva, "Properties and emerging applications of self-assembled structures made from inorganic nanoparticles," Nat. Nanotechnol. **5**, 15 (2009).
[20] J. Trice, D. Thomas, C. Favazza, R. Sureshkumar, and R. Kalyanaraman, "Pulsed-laser-induced dewetting in nanoscopic metal films: Theory and experiments," Phys. Rev. B **75**, 235439 (2007).
[21] J. Diez and L. Kondic, "On the breakup of fluid films of finite and infinite extent," Phys. Fluids **19**, 072107 (2007).
[22] C. Cottin-Bizonne, S. Jurine, J. Baudy, J. Crassous, F. Restagno, and E. Charlaix, "Nanorheology: An investigation of the boundary condition at hydrophobic and hydrophilic interfaces," Eur. Phys. J. E **9**, 47 (2002).
[23] R. Pit, H. Hervet, and L. Leger, "Direct experimental evidence of slip in hexadecane: Solid interfaces," Phys. Rev. Lett. **85**, 980 (2000).
[24] P. Joseph and P. Tabeling, "Direct measurement of the apparent slip length," Phys. Rev. E **71**, 035303 (2005).
[25] S. Afkhami and L. Kondic, "Numerical simulation of ejected molten metal nanoparticles liquified by laser irradiation: Interplay of geometry and dewetting," Phys. Rev. Lett. **111**, 034501 (2013).
[26] M. Fuentes-Cabrera, B. Rhodes, J. Fowlkes, A. López-Benzanilla, H. Terrones, M. Simpson, and P. Rack, "Molecular dynamics study of the dewetting of copper on graphite and graphene: Implications for nanoscale self-assembly," Phys. Rev. E. **83**, 041603 (2011).
[27] S. Popinet, The Gerris flow solver, 2012. 1.3.2, http://gfs.sourceforge.net/.
[28] S. Popinet, "An accurate adaptive solver for surface-tension-driven interfacial flows," J. Comput. Phys. **228**, 5838 (2009).
[29] R. Scardovelli and S. Zaleski, "Direct numerical simulation of free-surface and interfacial flow," Annu. Rev. Fluid Mech. **31**, 567 (1999).

This article is copyrighted as indicated in the article. Reuse of AIP content is subject to the terms at: http://scitation.aip.org/termsconditions. Downloaded to IP: 128.235.83.176 On: Mon, 21 Sep 2015 16:48:41

[30] E. Aulisa, S. Manservisi, R. Scardovelli, and S. Zaleski, "Interface reconstruction with least-square fit and split Eulerian-Lagrangian advection," J. Comput. Phys. **225**, 2301 (2007).
[31] S. Afkhami and M. Bussmann, "Height functions for applying contact angles to 3D VOF simulations," Int. J. Numer. Methods Fluids **61**, 827 (2009).
[32] M. Francois, S. Cummins, E. Dendy, D. Kothe, J. Sicilian, and M. Williams, "A balanced-force algorithm for continuous and sharp interfacial surface tension models within a volume tracking framework," J. Comput. Phys. **213**, 141 (2006).
[33] M. Sussman, "A second order coupled level set and volume-of-fluid method for computing growth and collapse of vapor bubbles," J. Comput. Phys. **187**, 110 (2003).
[34] M. Torrey, L. Cloutman, R. Mjolsness, and C. Hirt, "NASA-VOF2D: A Computer Program for Incompressible Flows with Free Surfaces," Tech. Rep. LA-10612-MS, Los Alamos Nat. Lab., 1985.

This article is copyrighted as indicated in the article. Reuse of AIP content is subject to the terms at: http://scitation.aip.org/termsconditions. Downloaded to IP: 128.235.83.176 On: Mon, 21 Sep 2015 16:48:41